LANGMUIR

pubs.acs.org/Langmuir Article

Fabrication and Comparative Quantitative Analysis of Plasmonic-Polymer Nanocomposites as Optical Platforms

Casey Folks, Uttam Sharma Phuyal, Mahima Rajesh, Nagathushara Arja, Michael Gladden, Logan Hamm, and Agampodi Swarnapali De Silva Indrasekara*



Cite This: Langmuir 2021, 37, 12853-12866



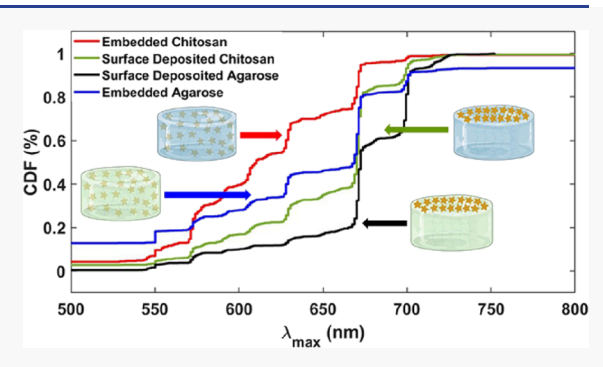
ACCESS I

III Metrics & More

Article Recommendations

s Supporting Information

ABSTRACT: Plasmonic-polymer nanocomposites can serve as a multifunctional platform for a wide range of applications such as biochemical sensing and photothermal treatments, where they synergistically benefit from the extraordinary optical properties of plasmonic nanoparticles (NPs) and biocompatible characteristics of biopolymers. The field translation of plasmonic-polymer nanocomposites requires design rules for scalable and reproducible fabrication with tunable and predictable optical properties and achieving the best performance. The optical properties of NPs and the optimal analytical performance of nanocomposites could be affected by many fabrication parameters, but a fundamental understanding of such parameters is still minimal. Herein, we systematically investigated the NP distribution and their optical properties



in gold nanostar (GNS)-polymer nanocomposites as a function of GNS concentration, polymer identity, and the method of GNS incorporation into a polymer matrix. We performed a comprehensive analysis of the single-particle scattering spectra of GNS incorporated into agarose gel and chitosan hydrogels via embedding and surface deposition, using dark-field spectroscopy. While relative GNS concentration affects the GNS scattering property distribution in both polymer matrices, chemical interactions between a polymer matrix and GNS is the key determinant of the GNS stability and homogenous distribution in nanocomposites. When GNS are embedded in a polymer matrix and there are stronger chemical interactions between GNS and a polymer, significantly less aggregation and a more homogenous distribution of GNS, which leads to a larger percentage of GNS optical property preservation, were observed at all the concentrations. In a proof-of-concept surface-enhanced Raman spectroscopy (SERS) study, we observed that the SERS detection efficiency is dictated by the analyte accessibility of GNS, which is governed by the polymer matrix porosity, polymer-GNS interactions, and other polymer physical characteristics. This work presents the interplay between key fabrication parameters and foundational design parameters for more predictable and reliable fabrication of plasmonic-polymer nanocomposites as an optical platform.

■ INTRODUCTION

The unique and extraordinary optical, physicochemical, and photothermal properties of plasmonic nanoparticles (NPs) have resulted in a wide range of highly promising imaging, sensing, and therapeutic applications. In particular, gold nanoparticles (AuNPs) and silver nanoparticles (AgNPs) have been utilized for enhanced optical spectroscopy-based applications, such as surface-enhanced Raman spectroscopy (SERS)- and dark-field scattering (DFS) spectroscopy-based biochemical sensing and imaging with high analytical sensitivity and specificity. The localized surface plasmon resonance (LSPR) of plasmonic NPs leads to the enhancement of the local electric near field around their surface, which can be tuned by changing the size and shape of the NPs and also their surrounding dielectric medium. The local environment sensitivity of plasmonic NP LSPR has been used for refractive index (RI)-based biochemical sensing, while the analyte-recognition-induced NP aggregation has been used for

plasmonic coupling-based probing of LSPR changes in UV—visible spectroscopy and in DFS spectroscopy as optical readouts in biochemical sensing and imaging. 9,10,13 However, scalable and reproducible production of plasmonic NP suspension-based optical platforms is a challenge.

Plasmonic NPs are incorporated into polymer matrices to design more user-friendly, highly robust, and flexible optical platforms while preserving the optical properties of plasmonic NPs. A wide range of plasmonic-polymer nanocomposites has been developed by combining AuNPs or AgNPs and polymers such as agarose, chitosan, and poly(methyl methacrylate)

Received: July 8, 2021
Revised: October 16, 2021
Published: October 27, 2021





(PMMA) for SERS-based optical sensing, imaging, and photothermal applications. 9,16–24 Plasmonic-polymer nanocomposites can synergistically benefit from the excellent optical properties of plasmonic NPs and the wide range of mechanical and chemical properties of polymers, rendering various functionalities. 25,26 For instance, plasmonic nanocomposites of macroporous poly-N-isopropylacrylamide (pNI-PAM) hydrogel loaded with gold nanorods have been used as biocompatible, SERS substrates for label-free in situ probing of quorum sensing in biofilms.9 Chitosan complexed with plasmonic NPs have been widely used as biocompatible optical substrates due to their excellent biocompatibility, biodegradability, and non-toxicity. 18,23,27-32 Xu et al. have developed stable and biocompatible Raman-active probes by coating gold nanoflowers (AuNFs) with chitosan and demonstrated their potential for targeting tumors in vivo.²⁸ Potara et al. have demonstrated the trace analysis of Ltryptophan (10⁻³ M) and single-molecule detection of adenine $(12 \times 10^{-12} \text{ M})$ using chitosan films embedded with AuNPs and AgNPs, respectively.^{23,27} Agarose-AgNPs nanocomposites have been demonstrated for reproducible and ultra-trace SERS detection of analytes as well as for recyclable molecular trapping and highly sensitive SERS detection of analytes such as dichlorodiphenyl-trichloroethane (10⁻⁸ M).^{21,33}

The field translation of plasmonic-polymer nanocomposites requires design rules for scalable and reproducible fabrication with tunable and predictable optical properties. Optical properties and the aggregation status of plasmonic NPs in polymer nanocomposites are critical for the reliability of their analytical performance. Plasmonic nanocomposites have been mostly characterized qualitatively using electron microscopy or reflectance spectroscopy, and only a very few studies have quantitatively characterized the optical properties of plasmonic NPs in polymer matrices. 16,34 For instance, Novo et al. have studied the influence of the surrounding medium RI on the optical properties of individual gold triangular prisms within a polymeric film.³⁵ They observed that the method of sample preparation greatly influences the polymer-AuNP substrate sensitivity, where the LSPR of AuNPs redshifts as the RI of the polymer matrix increases and spin coating polyvinyl alcohol (PVA) on glass and quartz plasmonic substrates decreases its analytical sensitivity. 35 Contreras-Cáceres et al. have reported that for pNIPAM encapsulated AuNPs, as the temperature of the dispersion increases, the RI increases, resulting in a redshift and absorbance increase of the LSPR of AuNPs.²⁰ While the optical properties of NPs and optimal analytical performance of nanocomposites could be affected by many fabrication parameters, a fundamental understanding of such parameters is still minimal. The advancement in the field of plasmonicpolymer nanocomposites desperately needs systematic and comprehensive investigations and a fundamental understanding of the optical properties of plasmonic NPs in nanocomposites and their impact on sensitive and reproducible optical readouts in sensing and imaging applications.

In this report, we systematically investigated the optical properties of plasmonic-polymer nanocomposites by analyzing the scattering properties of gold nanostars (GNS) as a function of GNS concentration, polymer identity, and nanocomposite configuration. We used surfactant-free GNS as the plasmonic NP of interest, as they have widely been used for biomedical applications due to their extraordinary scattering properties. 5,7,15,36,37 Agarose gel and chitosan hydrogel, two commonly used polymers as bioscaffolds, and two methods

of NP incorporation into polymers, surface deposition and embedding, were investigated to understand the effect of polymer identity and nanocomposite configuration on the stability, distribution, and scattering properties of GNS. 16,31,33,38 We performed a comprehensive analysis of the single-particle scattering spectra of GNS in nanocomposites at varying GNS-to-polymer volume concentrations using DFS spectroscopy. Scanning electron microscopy (SEM) and DFS microscopy images were used as secondary evidence of GNS distribution and aggregation patterns. While relative GNS concentration affects the GNS scattering property distribution in both polymer matrices, chemical interactions between the polymer matrix and GNS play a critical role in the stability and homogenous distribution of GNS in nanocomposites. We observed that nanocomposite preparation by the surface deposition of GNS leads to a higher degree of aggregation and shows less homogenous GNS distribution regardless of the polymer identity. In a proof-of-concept SERS study using nanocomposites fabricated under optimal conditions, we observed that the SERS detection efficiency is dictated by the analyte accessibility of GNS, which is governed by the polymer matrix porosity, polymer-GNS interactions, and other polymer physical characteristics.

■ EXPERIMENTAL SECTION

Chemicals and Materials. Gold(III) chloride trihydrate, sodium citrate tribasic dihydrate, gold chloride solution, hydrochloric acid (1.0 N), silver nitrate (AgNO₃), L-ascorbic acid (AA), chitosan (medium MW), sodium hydroxide (NaOH), and rose bengal (RB) were purchased from Sigma-Aldrich. Thiol-functionalized methoxy poly(ethylene glycol) (mPEG-SH) 1000 was purchased from Nanocs Inc. LB agar powder and Nile red (NR) were purchased from Thermo Fisher Scientific, and acetic acid (1.0 M) was purchased from Ward's Science. Ultrapure Millipore Milli-Q water was used for all syntheses. Prior to synthesis, the magnetic stir bars and glassware used in AuNP syntheses were aqua regia cleaned.

Surfactant- and Capping-Agent-Free GNS Synthesis. The GNS synthesis was performed using a modified version of De Silva Indrasekara $et\ al.^{15,44}$ First, in a 20 mL glass scintillation vial (VWR) containing a small magnetic stir bar, 10 mL of Milli-Q water was added and stirred at 580 rpm to form a steady vortex. Under ambient conditions, 492 μ L of gold chloride solution (5.08 mM) was added and mixed for 10 s. Then, 20 μ L of HCl (1.0 N) was added and mixed for 10 s. Immediately following, 173 μL of spherical AuNPs with a diameter of 14.9 \pm 1.4 nm as seeds (synthesis and characterization is provided in the Supporting Information, Figures S1 and S2) was added and mixed for 10 s. Next, 34 µL of AgNO₃ (3.0 mM) was added and mixed for 5 s. Immediately after the addition of AgNO₃, the formation of GNS begins, which is confirmed by a noticeable color change from colorless to navy blue. Thereafter, 100 μ L of AA (100 mM) was added and mixed for 60 s. Lastly, for long-term stability, 40 µL of mPEG-SH-1000 (1.0 mg/mL) was added and mixed for 10 min. The GNS were purified by centrifugation at 3000g for 10 min, and the resultant pellet was resuspended in 2.0 mL of Milli-Q water and stored at 4 °C. The stock solution of GNS had an LSPR wavelength maximum (λ_{max}) at 638 nm, an absorbance of 1.4, and a concentration of 0.03 nM. The calculation of GNS concentration is provided in the SI. The amount of m-PEG-SH-1000 required to achieve 40% GNS surface coverage was determined by using the average surface area of a GNS particle as determined by TEM imaging and the footprint of a PEG molecule of 0.35 nm².

Agarose Synthesis. In a 20 mL glass scintillation vial, 208.8 mg of LB-agar (32 mg/mL) was diluted with 6.53 mL of Milli-Q water and gently shaken by hand. A VWR hotplate was set to 130 °C, and the agar solution was heated and maintained around 120–130 °C. After 15 min, the solution began to gently boil. Once all of the agar powder was completely dissolved and the solution turned transparent,

the 20 mL glass scintillation vial containing agar solution was removed from the hot plate and allowed to cool until complete gelation was achieved (gelation time is roughly 15–20 min).

Gold Nanostars (LSPR: 638 nm, 0.03 nM) Embedded inside Agarose. The agar solution was first prepared as previously described. Four different GNS-embedded agarose samples were prepared at varying GNS-to-agar volume-to-volume (v/v%) concentrations (10, 15, 25, and 50%). Note that the volume fractions are describing the fraction of 0.03 nM GNS stock solution added to the polymer solution. Calculation of the concentration of the GNS stock solution and the total number of GNS particles in a given polymer substrate are provided in the SI. While the agarose mixture was heated to 120-130 °C, corresponding volumes of stock GNS solution (Table S1), were aliquoted into 2 mL microcentrifuge tubes. Then, the microcentrifuge tubes were placed in the thermal shaker, which is set at 40 °C. The microcentrifuge tubes containing GNS were warmed in the thermal shaker prior to adding agar solution because of how fast agar turns into a gel. The heated agar solution was removed from the heat and cooled to 40 °C, and then the corresponding volumes of agar solution, for each condition in Table S1, were quickly aliquoted into the corresponding 2 mL microcentrifuge tubes and mixed at 700 rpm for 1.5 h. After 1.5 h, the shaking speed of the thermal shaker was reduced to a manageable speed (450-500 rpm), and a temperature around 40 °C was maintained (Supporting Information, Figure S3) to prevent the embedded agar solution from turning into a gel immediately. Then, about 20 μL of the embedded agar solutions for each condition was pipetted directly from the microcentrifuge tubes, in the thermal shaker, and placed onto VWR premium precleaned glass slides (cat. no. 48300-048). The slides containing samples of GNS-embedded agar were covered immediately in a petri dish and dried for at least 1.5 h before DFS imaging. Five replicates of each condition (10, 15, 25, and 50%) were measured using DFS.

Gold Nanostars (LSPR: 638 nm, 0.03 nM) Surface-Deposited atop of Agarose. To surface-deposit GNS atop agarose, the agar solution was first prepared as previously described. Four different GNS surface-deposited agarose samples were prepared at varying GNS-to-agar v/v% concentrations (10, 15, 25, and 50%). Once the agar solution was completely dissolved under a gentle boil, corresponding volumes of agar solution (Table S1) were transferred onto glass slides and permitted to dry for 1.5 h at which the gelation of agarose was completed. Then, representative volumes of stock GNS solution, for each GNS concentration condition (Table S1), were pipetted directly on top of the agarose sample on the glass slide. The samples were dried for at least 1.5 h before DFS imaging. Five replicates of each condition (10, 15, 25, and 50%) were measured using DFS.

Chitosan Hydrogel Synthesis. Chitosan hydrogel was prepared according to Rami et al.45 Aqueous chitosan solution was prepared at a concentration of 2.6% (w/v). The degree of acetylation was in reference to Rami et al. using 5% (v/v) acetic acid. 45 The chitosan solution was vortexed on high for 60 s followed by centrifugation at 1000g for 15 min. After centrifugation, the mixture was vortexed on high for 60 s and sonicated for 15 min. The purity of the solution should become noticeable after the first round of purification. The same process of vortex, centrifugation, vortex, and sonication was repeated a second time for further purification of the chitosan solution. Chitosan solution was then poured into the mold and submerged inside a coagulation bath containing 10% (w/v) NaOH for 24 h. The amount of NaOH used in the coagulation bath was in excess to ensure more than complete coverage of the chitosan solution in order for gelation to occur throughout. After 24 h, the gelation of chitosan was completed, and the chitosan hydrogel was removed from the coagulation bath and then rinsed 2-3 times with Milli-Q water (Schematic S1). In the case of chitosan hydrogel dehydrating, single droplets of Milli-Q water were added to rehydrate the gel.

Gold Nanostars (LSPR: 638 nm, 0.03 nM) Embedded inside Chitosan Hydrogel. To make chitosan hydrogel embedded with GNS, the chitosan solution was prepared as previously described prior to the coagulation bath. Four different GNS-embedded chitosan

samples were prepared at varying GNS-to-chitosan v/v% concentrations (10, 15, 25, and 50%). Once the chitosan solution was purified, 0.50 mL of chitosan solution was aliquoted into four 2 mL microcentrifuge tubes. Corresponding volumes of stock GNS solution, for each GNS volume-by-volume concentration condition (Table S2), were aliquoted into the microcentrifuge tubes. The microcentrifuge tubes were vortexed on high for 2 min to disperse the GNS into the chitosan solution and then placed into the thermal shaker at 40 °C, shaking at 750 rpm for 1.5 h. Then, the mixture was pipetted in equally sized droplets onto glass slides and submerged in a coagulation bath containing 10% (w/v) NaOH for 24 h. After gelation was complete, the GNS-embedded hydrogel samples were gently rinsed 2–3 times with Milli-Q water to remove excess NaOH and allowed to dry for 4 h before DFS imaging. Five replicates of each condition (10, 15, 25, and 50%) were measured using DFS.

Gold Nanostars (LSPR: 638 nm, 0.03 nM) Surface-Deposited atop of Chitosan Hydrogel. Four different GNS-embedded chitosan samples were prepared at varying GNS-to-chitosan v/v%concentrations (10, 15, 25, and 50%). To surface-deposit GNS atop chitosan hydrogel, the chitosan solution was prepared as previously described. Once the chitosan solution was purified, equally sized droplets of chitosan solution were pipetted onto glass slides and submerged in a 10% (w/v) coagulation bath for gelation as described above. The hydrogel droplets were gently rinsed 2-3 times with Milli-Q water to remove excess NaOH and left to dry for 4 h. Then, representative volumes of stock GNS solution (Table S2) were added directly on top of the chitosan hydrogel samples, on the glass slide, and allowed to dry for at least 4 h before DFS imaging. Five replicates of each condition (10, 15, 25, and 50%) were measured using DFS. All five replicates were visibly checked to ensure that the hydrogel showed signs of hydration. In the case of dehydration, single droplets of Milli-Q were applied and allowed to dry before acquiring a DFS image. To ensure the reproducibility and accuracy of DFS and SERS characterization, the nanocomposites were hydrated prior to the introduction of the Raman-active molecules ensuring their even dispersion across and within the nanocomposite and exhibiting no visible signs of dehydration.

CHARACTERIZATION

UV–Visible Spectroscopy. The synthesized AuNPs and GNS were analyzed by UV–visible spectroscopy with the NanoDrop OneC spectrometer from Thermo Fisher Scientific (Figure S4). Using a plastic cuvette, 1.0 mL of solution was measured with a path length of 10 mm. The Lambert–Beer law equation was used to determine the concentration of the AuNPs and GNS. ⁴⁶

Transmission Electron Microscopy (TEM). The morphology of AuNPs and GNS was evaluated using a JEOL 2100 LaB6 transmission electron microscope. A total of 7.0 μ L of diluted AuNPs and GNS were drop casted onto a carbon-coated copper grid from Electron Microscopy Sciences.

Dark Field Scattering Spectromicroscopy. Cytoviva's hyperspectral imaging spectrometer was used for single-particle analysis. All of the samples were previously prepared on glass slides. The thicknesses of GNS-embedded and surface-deposited agarose and chitosan samples were kept less than 1.0 mm for DFS analysis (Figure S5). Micro-Manager, an open-source microscopy software, was used to acquire two fields of view (696 × 348 pixels) for five replicates of each condition (10, 15, 25, and 50%), with an exposure time of 200 ms using 60× oil objective (NA 1.25). Spatial and spectral information of the enhanced dark-field hyperspectral image were obtained using Environment for Visualization (ENVI) 4.8 software. Additional fields of view were acquired, for each replicate, if the total particle counts were below 1000–3000 counts.

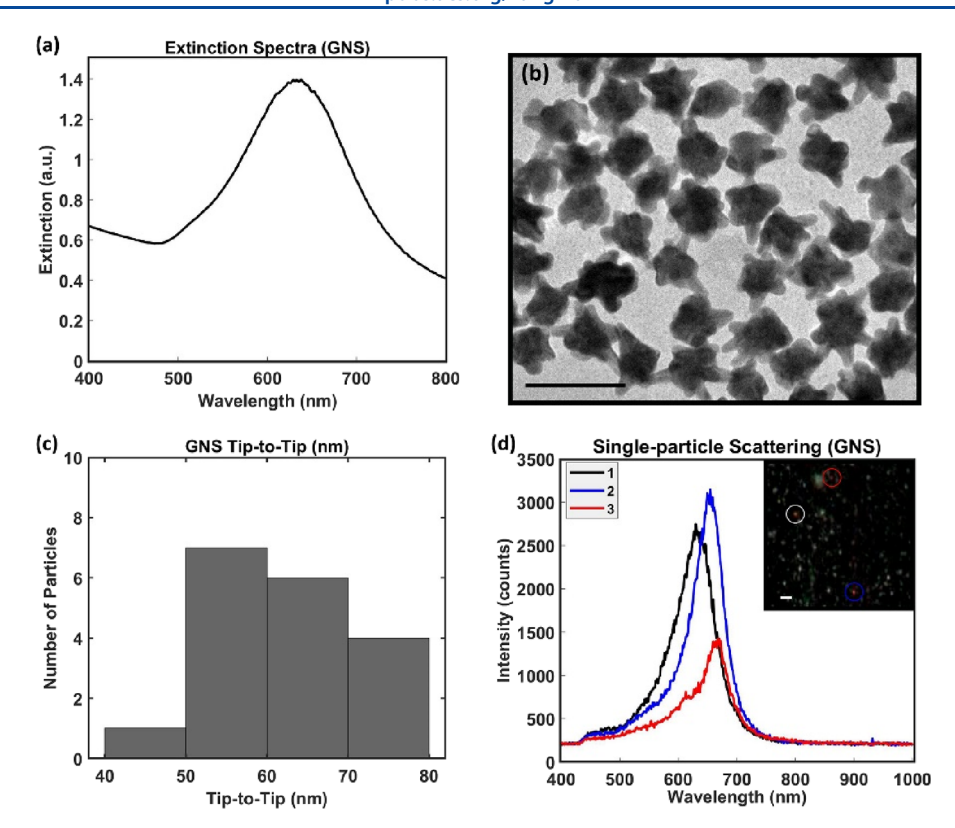


Figure 1. Characterization of surfactant-free GNS for the fabrication of plasmonic-polymer nanocomposites. (a) Representative ensemble UV–visible extinction spectrum of GNS showing a λ_{max} of 638 nm. (b) Representative TEM micrograph confirmed the branched-like morphology and a high yield synthesis of GNS (scale bar: 100 nm). (c) The distribution of the tip-to-tip diameter of GNS (61.0 \pm 7.8 nm) as determined by TEM micrograph analysis shows surfactant-free GNS batch with high monodispersity. (d) Representative DFS image of GNS (scale bar = 10 μ m) and single-particle scattering spectra of three individual GNS exhibiting λ_{max} within 630–650 nm range.

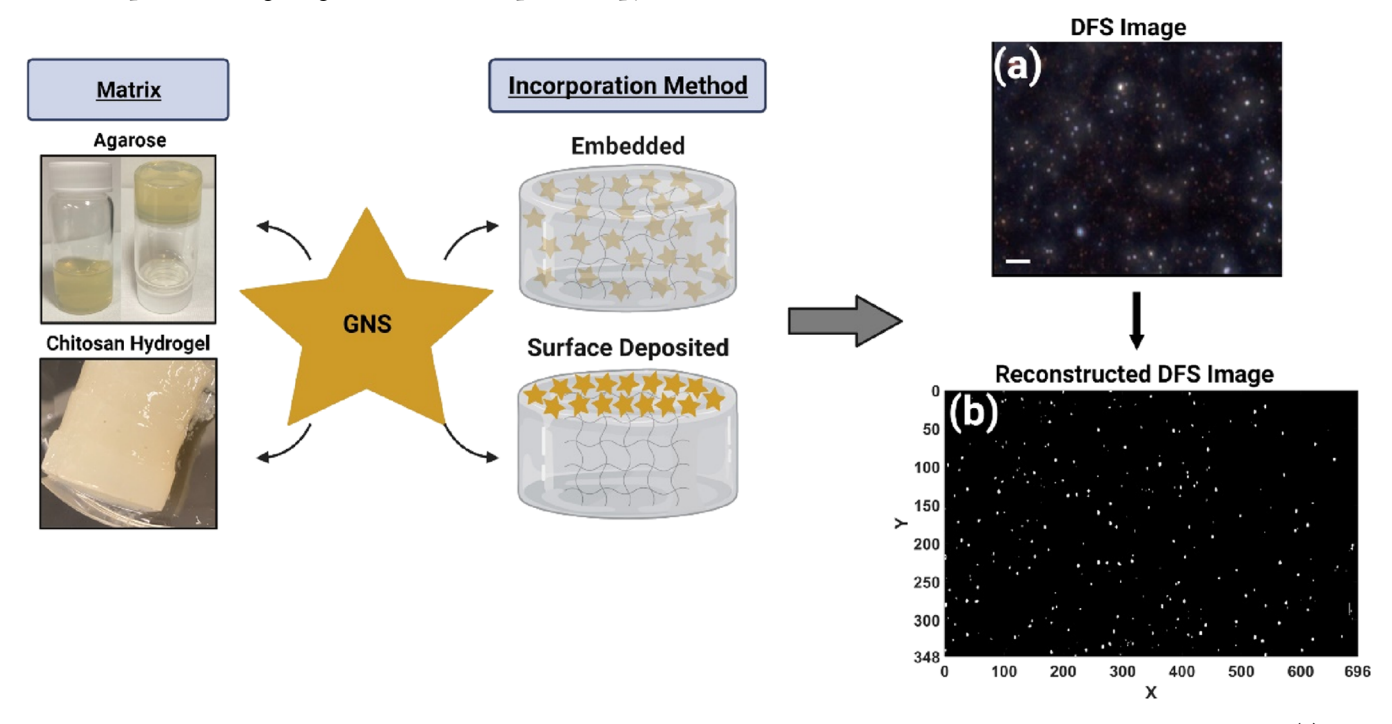
Dark-Field Image Reconstruction and Single-Particle Analysis. The enhanced dark-field hyperspectral images acquired using the Cytoviva's hyperspectral imaging spectrometer contain three dimensions, two spatial and one spectral dimension, producing a hyperspectral data cube. The spectral data of each hypercube was further processed using MATLAB ver. R2020a (MathWorks Inc., USA). Briefly, the MATLAB program extracted the spectral profile at each pixel of the dark field image. Spectral and spatial conditions were applied to the hyperspectral data to filter the particles that contained a minimum intensity (photon counts) of 1000 and a maximum intensity (photon counts) of 5000. Filtering out particles with an intensity below 1000 counts or above 5000 counts removed any low scattering pixels, aggregates, and highscattering pixels that would alter the data conclusions. Furthermore, any particles greater than 20 connected pixels were filtered out. From the MATLAB code, single histograms of the λ_{max} (Figures S6–S9) were individually plotted for each replicate hypercube (Schematic S2). The individual histograms were combined to produce a cumulative histogram for GNSembedded and GNS surface-deposited agarose and chitosanembedded hydrogel. The MATLAB built-in CDF function was used with the cumulative λ_{max} data for each sample, and the Kolmogorov-Smirnov test was performed on MathWorks to determine the statistical difference between all the conditions compared in this study (Figures 2 and 3).

Scanning Electron Microscopy (SEM). The optimized conditions of GNS-embedded and GNS surface-deposited agarose and chitosan hydrogel were deposited on Silicon wafers and imaged using an Apreo S by ThermoFisher

Scientific scanning electron microscope. The SEM images were taken with a tilt angle of 0.0° and an accelerating voltage of $12.0~\rm kV$. The SEM images were taken at a magnification of $10,000\times$ (full fields of view) and $100,000\times$ (inset images). Charging was a major problem in imaging both GNS-agar and GNS-chitosan nanocomposites; therefore, lower magnifications were used for imaging at the expense of image quality and resolution to ensure no sample modification during SEM imaging.

SERS Analysis. HORIBA Scientific's XploRA Raman microscope system integrated with Cytoviva's hyperspectral imaging spectrometer was used for SERS analysis. The optimized conditions of GNS-embedded and GNS surfacedeposited agarose and chitosan hydrogel on glass slides were used for SERS analysis. After at least 4 h of drying, 1.0 μ L of RB (10^{-4} M) was added to the top of the nanocomposites. Horiba LabSpec6 software was used for SERS Mapping using a 638 nm laser, 10× objective, 600 grating, slit size of 100 μ m, hole size 300 μ m, and SWIFT mode at every line, with a map size of 20 μ m \times 20 μ m (step size 16.2 \times 17), an acquisition time of 0.25 s, and a 1.0 accumulation. SERS maps were reconstructed using a MATLAB program. Average SERS response of a given nanocomposite with no analyte (blank) was taken as the background noise and subtracted from the SERS response of the corresponding nanocomposite in the presence of the analyte (Figures S10 and S11). The average SERS/Raman signal intensities reported in this manuscript, both in SERS spectra (Figures S12 and S13) and SERS maps (Figure 6) are background-subtracted.

Scheme 1. Overview of the Workflow for Fabricating GNS-Polymer Nanocomposites and Optical Characterization of GNS in Nanocomposites Using Single-Particle DFS Spectroscopy^a



"Nanocomposites were fabricated by dispersing GNS in agarose and chitosan hydrogel matrices via embedding and surface deposition. (a) DFS image of GNS-polymer nanocomposites and (b) reconstructed DFS image used in the analysis of GNS for the distribution of GNS and their scattering properties as a function of GNS concentration, polymer matrix type, and the method of GNS incorporation into nanocomposites

Normalized and background-subtracted SERS intensity at a $1616 \, \mathrm{cm}^{-1}$ Raman shift of RB was used to construct SERS maps at two different concentrations (10^{-4} and 10^{-5} M) of RB (Figures S14 and S15). The SERS maps were reconstructed in MATLAB. Briefly, a surface plot of X and Y spatial coordinates were drawn and the SERS peak intensity at $1616 \, \mathrm{cm}^{-1}$ at each XY coordinate was superimposed on the XY surface plot. The intensity variation was represented in terms of variation in color on the scale bar.

In addition, the same procedure was followed using Nile red (NR) (10^{-4} M) , to assess and compare the performance of nanocomposites in detecting hydrophobic analytes. SERS maps of NR were reconstructed using a MATLAB program. The normalized and background-subtracted SERS intensity at 1487 cm $^{-1}$ Raman shift of NR was used to construct the SERS maps (Figures S16 and S17).

■ RESULTS AND DISCUSSION

Fabricating Plasmonic-Polymer Nanocomposites.

The plasmonic-polymer nanocomposites were developed by incorporating surfactant-free GNS into agar and chitosan matrices. GNS have been used as highly efficient and sensitive substrates in LSPR- and SERS-based imaging and sensing applications due to the larger scattering cross section of individual GNS, their larger near-field enhancement that arises from their sharp features compared to spherical AuNPs, and also AuNP aggregation-based "hotspots". Therefore, in this study, we used GNS as the plasmonic NP of interest. In particular, the GNS used in this study was synthesized using a surfactant-free route due to their proven biocompatibility, ease of synthesis, and surface functionalization for biomedical sensing and imaging applications. ¹⁵ Surfactant-mediated GNS

synthesis usually involves a difficult process for the removal of surfactants, and limited access of analytes for surface functionalization. 39 In this study, GNS with an LSPR (λ_{max}) of 638 nm (1.4 a.u., 0.03 nM) (Figure 1a) were synthesized to align them in resonance with a 638 nm laser excitation and thereby to investigate the effectiveness of plasmonic nanocomposites as SERS substrates used in a proof-of-concept study. Surfactant-free GNS were first synthesized using a seed-mediated growth method (Figure S1), ¹¹ and were then surface functionalized at 40% coverage using mPEG-SH to ensure long-term colloidal stability, thereby ensuring the retention of the optical properties of the as-synthesized GNS in solution over time. A low surface coverage of mPEG-SH on GNS will allow sufficient GNS surface area for any other molecular interactions and any further surface functionalization. The morphology of GNS, which is characterized by sharp tips protruding from a spherical core was confirmed by TEM (Figure 1b) with an average tip-to-tip diameter of 61.0 nm ± 7.8 (Figure 1c and Figure S2), which agrees well with that of the surfactant-free GNS with an $\lambda_{\rm max}$ of 630–638 nm reported by De Silva Indrasekara *et al.*¹⁵ The DFS spectroscopy under hyperspectral imaging conditions (Figure 1d) was used to characterize the scattering properties of a statistically significant population of GNS at the single-particle level, prior to using them to develop plasmonic nanocomposites. The individual scattering spectra of GNS showed scattering λ_{max} in the range of 630–650 nm (Figure 1d).

In a plasmonic nanocomposite, the observed scattering λ_{max} of NPs and λ_{max} distribution is a function of the RI of its surrounding (polymer matrix) and the aggregation status of plasmonic NPs, respectively, which in turn affects the reliability of their optical response in optical sensing and imaging

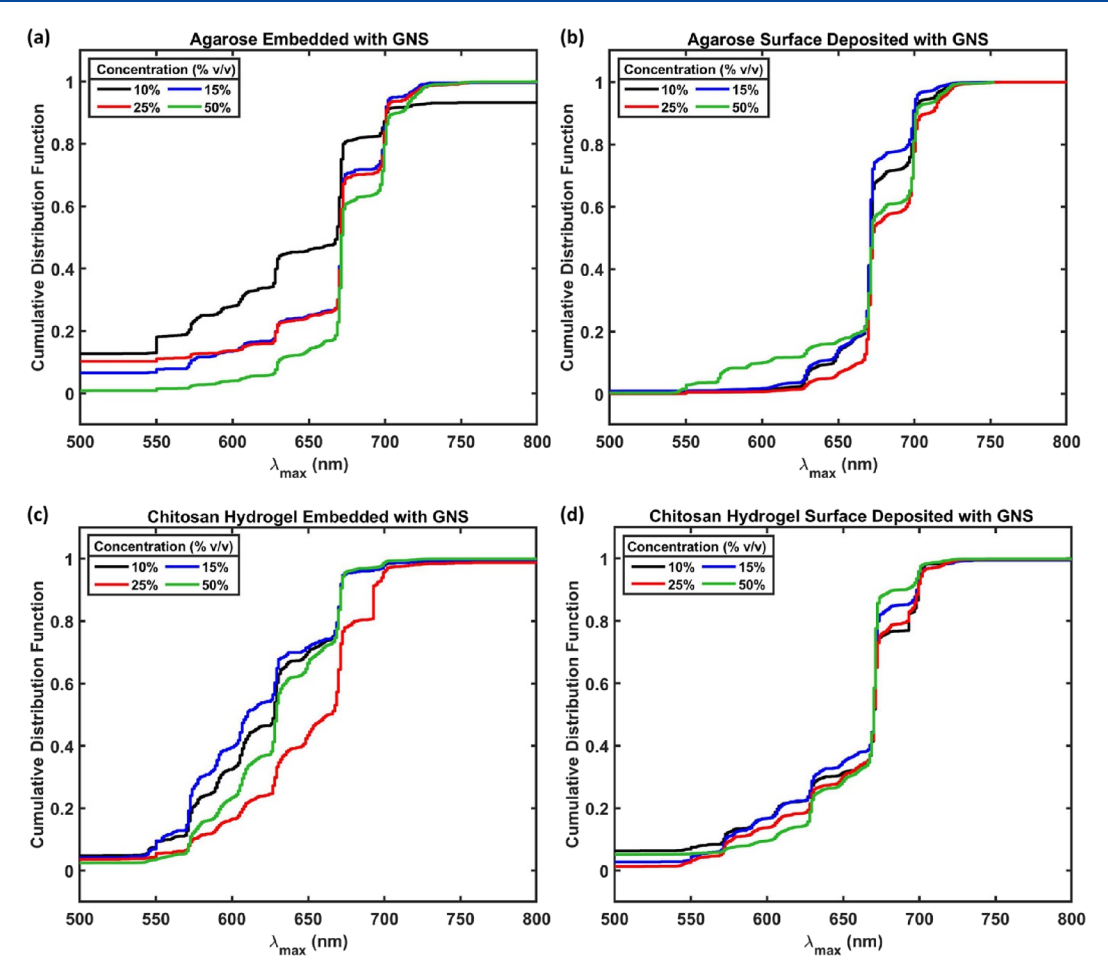


Figure 2. The scattering properties of GNS in a polymer nanocomposite is dictated by the polymer chemistry and the method of GNS incorporation into the polymer matrix, while the relative GNS concentration is also a significant contributing factor. CDF plots of scattering $\lambda_{\rm max}$ for (a) GNS-embedded agarose, (b) GNS surface-deposited in agarose, (c) GNS-embedded chitosan hydrogel, and (d) GNS surface-deposited in chitosan hydrogel. 10% (v/v) GNS-embedded agarose, 50% (v/v) GNS surface-deposited agarose, and both 15% (v/v) GNS-embedded and GNS surface-deposited chitosan hydrogel shows the highest percentage of GNS exhibiting scattering properties within 600–700 nm in the respective nanocomposite categories.

applications.³⁵ Therefore, it is of great importance to identify how the polymer matrix type, GNS concentration, and method of GNS incorporation into a polymer matrix could influence the stability, aggregation status, and the scattering $\lambda_{\rm max}$ of GNS. In this study, surfactant-free GNS with an average $\lambda_{\rm max}$ of 638 nm were incorporated into two polymer matrices: agarose and chitosan, using two different methods; GNS embedded into the matrix and GNS surface-deposited atop the matrix to understand the effect of these parameters on GNS distribution within a nanocomposite and the scattering properties of GNS.

Nanoparticle Concentration-Dependent Optical Properties of Gold Nanostar-Polymer Nanocomposites. Four plasmonic nanocomposite configurations; (1) GNS-embedded agarose, (2) GNS surface-deposited agarose, (3) GNS-embedded chitosan hydrogel, and (4) GNS surface-deposited chitosan hydrogel (Scheme 1), were investigated for the scattering properties of the associated GNS with respect to that in water. Scattering spectra of GNS at the single-particle level were collected from a statistically significant population using hyperspectral dark-field scattering spectroscopy. The concentration dependence was monitored by the change in the scattering $\lambda_{\rm max}$ of GNS, which was then used to determine the concentration dependence of the GNS scattering properties, the conditions for which a more homogenous distribution of

GNS scattering properties and a less deviation of the scattering properties of the original GNS can be obtained. The concentration of GNS in each nanocomposite configuration in terms of volume-to-volume GNS/polymer ratio (v/v%) at 10, 15, 25, and 50% were analyzed. Note that the volume fractions describe the fraction of 0.03 nM GNS stock solution added to the polymer solution (Experimental Section and SI). For an accurate representation of GNS scattering properties, at least two randomly selected fields of view for each replicate, for five replicates per each condition, were analyzed by screening a statistically large GNS population. Quantitative analysis of the concentration- and matrix-dependent scattering properties of plasmonic nanocomposites was done using elements of probability. Cumulative distribution function (CDF) plots were used to summarize λ_{max} of single GNS in nanocomposites over the entire spectral range of 500-800 nm and to accurately determine the percentage of GNS in nanocomposites exhibiting optical properties within a specific range of wavelengths. In CDF plots, the probability of GNS retaining their optical properties is interpreted as a percentage of particles below a certain λ_{max} . As the synthesized GNS use in this study exhibit an average λ_{max} of 638 nm, the 600–700 nm range was considered as the specific wavelength range of interest, and particles exhibiting scattering beyond that region

Table 1. Percentages of GNS Exhibiting λ_{max} within the Wavelength Regions of Interests and the Total Number of GNS Particle Count within the 500–800 nm Range for GNS-Agarose Nanocomposites^a

sample (GNS/agar v/v%)	probability of GNS exhibiting scattering at each wavelength range of interests (%)									
	GNS-embedded agarose				GNS surface-deposited agarose					
	10	15	25	50	10	15	25	50		
wavelength regions										
lower limit (600 nm)	25	15	15	5	1	2	1	10		
median limit (650 nm)	45	23	22	10	10	11	5	18		
upper limit (700 nm)	90	96	95	90	95	96	90	92		
above 700 nm	100	100	100	100	100	100	100	100		
total particle count	1566	797	1141	2226	10,770	6977	5579	1673		

[&]quot;The tabulated values are the probabilities predicted by CDF in Figure 2 as a percentage of particles exhibiting scattering with a given λ_{\max} up to the defined lower, median, and upper limits.

is considered subjected to morphological alterations such as aggregation. Within the wavelength range of interest, three wavelength limits were established as standards: (1) a lower scattering limit of 600 nm, (2) an upper scattering limit of 700 nm, and (3) a median point of 650 nm to quantitatively determine nanocomposite fabrication conditions that would minimally change the scattering properties of GNS when incorporated into agar or chitosan matrices. The Kolmogorov–Smirnov test was used to estimate any significant differences between variables.

Gold Nanostars Incorporated in Agarose. The GNS morphology and hence their optical properties could be affected by the elevated temperatures required during the GNS-agarose gel nanocomposite fabrication. To determine the optimal temperature for incorporating GNS into agarose, the temperature dependence of the GNS morphology and size distribution was investigated in water with respect to that at room temperature (21 °C). Based on the TEM image analysis and UV—visible spectra (Figure S3), the GNS morphology was deformed and led to aggregation when the temperature of the GNS surrounding medium was increased above 40 °C. Therefore, when fabricating GNS-agarose nanocomposites, GNS were added when agar solution reaches 40 °C and before it completes the gelation (Figure S4).

NP distribution and their scattering properties in GNSembedded and GNS surface-deposited agarose nanocomposites depend on the relative GNS concentration in nanocomposites. DFS measurements were acquired from 400 to 1000 nm, and only the 500-800 nm range is considered for further analysis using CDF. In GNS-embedded agarose gel, as the concentration (v/v%) of GNS increases, the percentage of GNS deviating from their original scattering peak position within 600–700 nm decreases (Figure 2a). λ_{max} histograms of GNS embedded agarose at all concentrations demonstrate a higher percentage of GNS still exhibiting scattering properties within 600-700 nm (Table 1 and Figures S6 and S7). CDF plots clearly demonstrate that a significant amount of GNS has red-shifted from the average λ_{max} of starting GNS (638 nm), which can be attributed to the RI change of the GNS local environment from air (1.00) to agarose (1.33).41 In 10% GNSembedded agarose, 45% of GNS retained λ_{max} around 650 nm, but it dropped to only 10% of GNS for 50% GNS-embedded agarose. At higher GNS concentrations, a significantly higher percentage of GNS with λ_{max} greater than 750 nm was observed at all the concentrations except 10% GNS. This observation can be also better explained by the shrink-swell properties of agarose, where the dehydration of agarose upon exposure to air leads to aggregate formation, thereby resulting

in a plasmonic "hot-spot" formation. Ma et al. have observed a similar phenomenon in AuNP-agarose nanocomposites prepared for SERS-based applications, where the nanocomposite volume decreases as the gel shrinks upon dehydration.³⁸ The gelation of agarose is created due to the presence of hydrogen bonds. The pore size of agarose is dependent on the relative concentration of agarose in the nanocomposite; thus, the higher the concentration of agarose, the smaller and denser the pores. As the relative concentration of NPs in a nanocomposite increases, the probability of NPs getting trapped within the agarose pores increases as well. During the drying process involved in agarose gel formation, the shrinkage of agarose could force GNS to move closer to each other, causing aggregate formation and plasmonic coupling between GNS particles, thereby contributing dominantly toward the observed λ_{max} . This explains the lowest GNS concentration in embedded agarose nanocomposites resulting in the highest percentage of GNS retaining λ_{max} within 600-700 nm. Based on the Kolmogorov-Smirnov test, it was determined that the GNS scattering λ_{max} distribution at each GNS concentration in embedded agar (10, 15, 25, and 50%) is significantly different from each other. This concludes the relative GNS concentration dependence of the overall scattering properties and relative uniformity of GNS distribution in GNS-embedded agar nanocomposites.

On the contrary to embedded agar, as the v/v% concentration of GNS in surface-deposited agarose is increased, the percentage of GNS retaining λ_{max} within 600-700 nm is increased (Figure 2b). The percentage of GNS exhibiting λ_{max} at or below 650 nm was increased from 10 to 18% when the concentration of GNS in surface-deposited agarose was increased from 10 to 50%. Further analysis of CDF plots reveals that 50% GNS surface-deposited agarose demonstrates a significantly higher percentage of GNS retaining the λ_{max} region of interest; at the lower limit (600 nm), median point (650 nm), and upper limit (700 nm), in comparison to the other three GNS concentrations. The fabrication of GNS surface-deposited agarose nanocomposites involves air drying of a colloidal suspension of GNS atop of agarose. There is a higher probability for GNS to aggregate via capillary action, as no strong chemical interactions hold them in place during the drying process involved in the nanocomposite formation. This process could explain the higher percentage of aggregates and also a higher percentage of GNS with λ_{max} above the upper limit (700 nm) than below the median point (650 nm), which is observed as the GNS concentration increases. Here, the relatively less GNS concentration dependence apparent in GNS surface-deposited

agarose in comparison to GNS-embedded agarose substrates could be therefore explained by the dominance of dying effect leading to NP aggregation.

Collectively, the distribution and the scattering properties of GNS in plasmonic-agarose nanocomposites are significantly affected by the methods of GNS incorporation, embedding in agarose vs surface deposition on agarose. In general, a relatively larger red shift in the average GNS $\lambda_{\rm max}$ is observed in embedded agarose than that in surface-deposited agarose at all concentrations (Figure 3). The average $\lambda_{\rm max}$ of GNS in

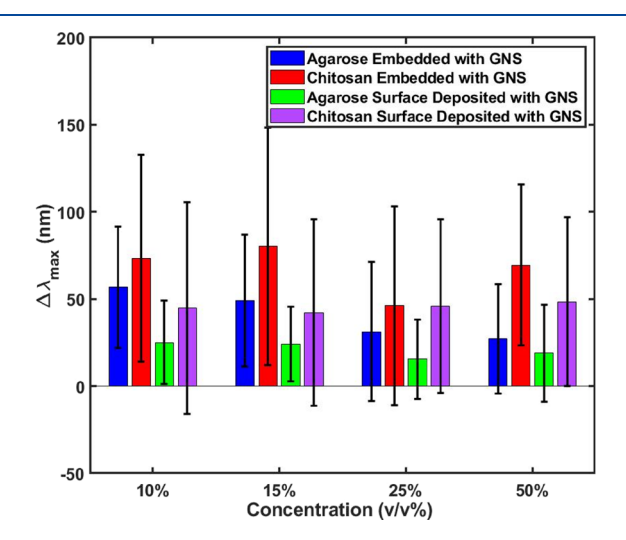


Figure 3. $\Delta\lambda_{\rm max}$ is the change in $\lambda_{\rm max}$ of GNS in the nanocomposites with respect to GNS in water ($\lambda_{\rm max}=638$ nm) at varying concentrations of GNS in the polymer matrix (v/v%). GNS-embedded chitosan resulted in the largest average $\Delta\lambda_{\rm max}$ while GNS surface-deposited agarose resulted in the smallest average $\Delta\lambda_{\rm max}$ at all the concentrations considered in this study. $\Delta\lambda_{\rm max}=\lambda_{\rm max\;(nanocomposite)}-\lambda_{\rm max\;(water)}$.

nanocomposites is influenced by the degree of aggregation and the effective RI experienced by NPs when they are embedded and surface-deposited in agarose and chitosan hydrogel. This could be explained by the differences in the effective local RI index experienced by GNS. In embedded agarose, GNS are fully immersed in agarose gel with effective RI equivalent to agarose, while GNS experience a relatively lower RI in surface-deposited nanocomposite as they are at the interface between agar and air. In general, GNS-embedded agarose resulted in a higher overall percentage of particles retaining scattering $\lambda_{\rm max}$ within 600–700 nm where the highest was observed at 10%

GNS. Embedding GNS into agarose allows GNS to dry simultaneously along with the gelation of agarose, and GNS distribution within agarose could be driven mainly by the entrapment of GNS via steric and chemical interactions and the restricted diffusion of spherical molecules within the cylindrical pores of agarose.⁴²

Gold Nanostars Incorporated in Chitosan Hydrogel. Both GNS-embedded and surface-deposited chitosan show a similar trend in GNS concentration dependence. For GNSembedded chitosan, at the median limit (650 nm), a larger variation in the percentage of particles retaining optical properties was observed. As the GNS concentration in embedded chitosan hydrogel increases, the percentage of particles retaining scattering properties at the median limit (600 nm) decreases, except for the 15% (v/v) concentration where a 30% increase in the percentage of particles was observed in comparison to 25% GNS-chitosan (Figure 2c and Table 2). All GNS concentrations resulted in relatively the same percentage of particles at the upper limit (700 nm). In comparison to GNS-agarose nanocomposites, this general trend of the inverse relationship between the percentage of GNS with λ_{max} within 600–700 nm and the concentration (v/v %) could be a result of chitosan hydrogel serving as an additional protective layer to the GNS.⁴³ As evident in the CDF plots, in general, for GNS surface-deposited chitosan, a clear decrease in the percentage of nanoparticles with λ_{max} at the lower limit (600 nm) can be observed as the GNS concentration in chitosan increases. The 10% surfacedeposited chitosan demonstrates a higher percentage of particles retaining λ_{max} at the lower limit (600 nm) and median point (650 nm) (Table 2, Figures S8 and S9) than the other GNS concentrations. While there is a significant difference between GNS concentration and the observed λ_{max} as determined by the Kolmogorov-Smirnov test, the relative difference is smaller compared to that of GNS-embedded chitosan. For instance, about 18% of GNS demonstrated $\lambda_{\rm max}$ at the lower limit for both 10 and 15% (v/v) concentrations, while it was only 10% of GNS at 50% (v/v) concentration. The 15% (v/v) GNS surface-deposited atop chitosan hydrogel was determined as the optimized condition because it demonstrated the highest percentage of particles (35%) retaining optical properties at the median wavelength point (650 nm).

Both 15% GNS-embedded and GNS surface-deposited chitosan shows the highest percentage of particles with $\lambda_{\rm max}$ within 600–700 nm for each nanocomposite configuration. A total of 70% and 35% of particles retained $\lambda_{\rm max}$ at the median point (650 nm) for both embedded and surface-deposited

Table 2. Percentages of GNS Exhibiting λ_{max} within the Wavelength Regions of Interests and the Total Number of GNS Particle Count within the 500–800 nm Range for GNS-Chitosan Nanocomposites^a

	probability of GNS exhibiting scattering at each wavelength range of interests (%)									
	GNS-embedded chitosan				GNS surface-deposited chitosan					
sample (GNS/chitosan v/v%)	10	15	25	50	10	15	25	50		
wavelength regions										
lower limit (600 nm)	36	40	28	22	18	18	15	10		
median limit (650 nm)	70	70	65	10	30	35	26	25		
upper limit (700 nm)	100	99	98	100	97	98	96	98		
above 700 nm	100	100	100	100	100	100	100	100		
total particle count	1324	553	1053	6007	2150	1348	2596	4098		

[&]quot;The tabulated values are the probabilities predicted by CDF in Figure 2 as a percentage of particles exhibiting scattering with a given λ_{\max} up to the defined lower, median, and upper limits.

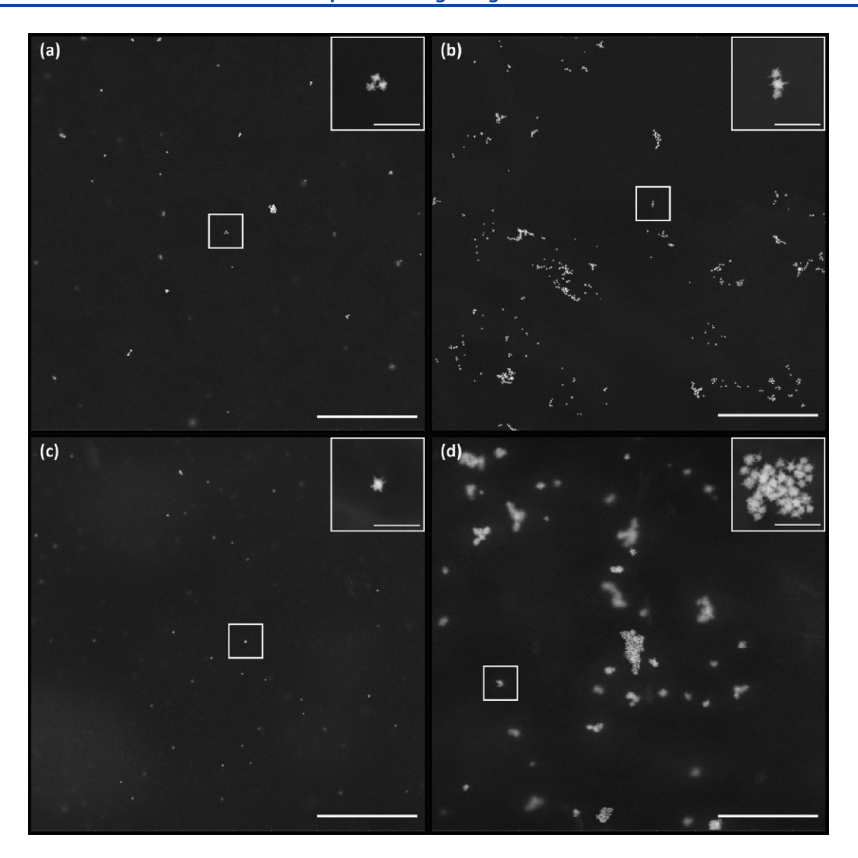


Figure 4. SEM micrographs show the retention of the overall branch-like GNS morphology in nanocomposites and the variation of GNS distributions in nanocomposites depending on the polymer chemistry and the method of GNS incorporation into polymer matrices. SEM micrographs of (a) 10% GNS-embedded agarose, (b) 50% GNS surface-deposited agarose, (c) 15% GNS-embedded chitosan hydrogel, and (d) 15% GNS surface-deposited chitosan hydrogel, which are the optimal conditions for each nanocomposite category that show the highest percentage of GNS exhibiting scattering properties within 600-700 nm (scale bar = 3 μ m, inset image scale bar = 300 nm).

chitosan, respectively. During nanocomposite fabrication, embedding GNS into chitosan solution allows the gelation to occur simultaneously while GNS is being stabilized via the formation of a surface protective chitosan layer, which is absent when GNS are surface-deposited to prevent them from mass aggregation. This could explain the less GNS aggregation and more uniform GNS distribution across nanocomposites, thereby leading to the observed higher percentage of GNS retaining $\lambda_{\rm max}$ within 600–700 in embedded chitosan. The lower percentage of GNS retaining $\lambda_{\rm max}$ within 600–700 nm in surface-deposited chitosan could be attributed to the competing forces at the GNS-chitosan interfaces: variable chemical interactions at the GNS and chitosan surface and GNS aggregation as a result of the drying effects.

Comparison of the Configuration and the Polymer Identity-Dependent Scattering Properties of GNS-Polymer Nanocomposites. Polymer matrix- and nanoparticle incorporation method-specific variations of GNS scattering properties and GNS distributions on a nanocomposite are evident in the four nanocomposite substrates at their optimal conditions. Figure 3 shows the average change in λ_{\max} ($\Delta\lambda_{\max} = \lambda_{\max}$ (nanocomposite) $-\lambda_{\max}$ (water)) of GNS in the nanocomposites with respect to GNS in water, which was used for nanocomposite fabrication. In general, the $\Delta\lambda_{\max}$ of both GNS surface-deposited and GNS-embedded chitosan nanocomposites are larger compared to that of GNS-agar nanocomposites. This observation can be attributed to the higher RI of the chitosan hydrogel than agarose and air, which leads to a larger overall redshift in λ_{\max} of individual GNS

nanoparticles. 35,41,42 The nanocomposites prepared by embedding GNS, regardless of polymer identity, show a larger $\Delta \lambda_{\rm max}$ than the surface-deposited GNS, which is reflected in the observed $\lambda_{\rm max}$. This observation can be explained by the different effective RI experienced by GNS. In surface-deposited nanocomposites, GNS at the interface of the polymer and air experience a lower effective RI than GNS completely surrounded by a polymer in embedded nanocomposites, which is subjected to a local RI similar to the polymer itself. 35,41,42

When comparing the matrix effect between the GNS surface-deposited nanocomposites, a relatively larger percentage of nanoparticles with λ_{max} over 700 nm were observed in agarose than in chitosan, at all the concentrations (v/v%) considered in this study. The upper λ_{max} limit (700 nm) was compared as a metric to assess the degree of nanoparticle aggregation. GNS used in this study had a 40% coverage of mPEG-SH, and a larger portion of the GNS surface (60%) is still available for weak covalent interactions with deprotonated, primary amines present on the chitosan surface. During the fabrication, chitosan hydrogel was rinsed off with Milli-Q water to remove NaOH before the deposition of GNS; however, there could be remaining NaOH providing a slightly basic surface that could enable favorable chemical interactions between chitosan and GNS. Therefore, we speculate that a balance between the drying effects forcing GNS to attract toward each other and GNS chemically interacting with primary amine groups of chitosan could lead to a lesser degree of aggregation within GNS-chitosan interactions. On the other

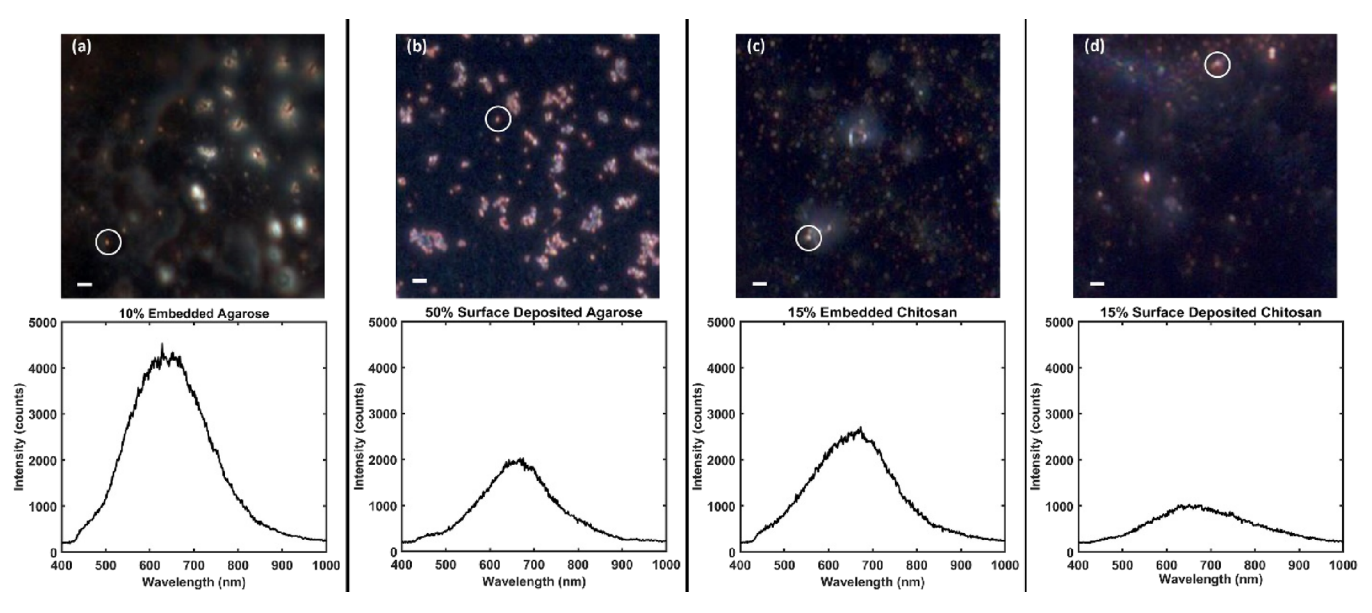


Figure 5. DFS images of nanocomposites show the GNS distribution patterns that reflect the average GNS scattering λ_{max} distribution observed at the single-particle level. Representative DFS images and single-particle scattering spectra of individual GNS for the four conditions that retained the highest percentage of GNS exhibiting scattering properties within 600–700 nm: (a) 10% embedded agarose, (b) 50% surface-deposited agarose, (c) 15% embedded chitosan hydrogel, and (d) 15% surface-deposited chitosan hydrogel. GNS-embedded agarose and chitosan hydrogel (a, c) resulted in GNS scattering intensities at least two times greater than that of agarose and chitosan hydrogel surface-deposited with GNS (b, d), respectively. DFS images show a significantly larger amount of GNS aggregates present in both GNS surface-deposited agarose and chitosan hydrogel (scale bar = 10 μ m).

hand, in GNS surface-deposited agarose, there are no such even weaker covalent interactions between agarose and GNS to hold them against drying effects.

When comparing the matrix effect between the GNSembedded nanocomposites, GNS-embedded chitosan demonstrates a relatively larger percentage of GNS at the median $\lambda_{\rm max}$ point of 650 nm and within 600-700 nm at all the concentrations (v/v%) than in agarose except at 10% GNSembedded agarose. In addition, a relatively larger percentage of nanoparticles with λ_{\max} over 700 nm was observed in agarose than in chitosan at all the concentrations considered in this study, which indicates a higher percentage of aggregation in agarose. Between the four configurations, 15% embedded chitosan resulted in the highest percentage of GNS retaining scattering properties within the 600-700 nm with less aggregation and more homogenous GNS distribution across the substrate. The lower percentage of particles retaining scattering properties within 600-700 in GNS surfacedeposited agarose and chitosan hydrogel concludes that nanocomposite fabrication via NP surface deposition does not provide a reliable and sensitive optically active nanocomposite. This can be attributed to the hydrogen bondingmediated GNS-chitosan interactions facilitating more stability in sol-gel media, which is lacking when agarose is used as a polymer matrix for plasmonic nanocomposite fabrication. While the changes in FWHM were compared, no significant trends in the FWHM changes or a relationship between the FWHM and the nanocomposite types were observed (data not

Characterization of Gold Nanostar Distribution in Nanocomposites by Scanning Electron Microscopy (SEM) and Dark-Field Scattering Microscopy Imaging. The distribution of GNS across the surface and within the nanocomposites revealed from the scanning electron microscopy (SEM) images and DFS spectroscopy images are in

agreement with the scattering properties of GNS in nanocomposites as indicated in CDF plots (Figure 2). SEM images show that the overall branch-like morphology of GNS remained unchanged in all the four nanocomposites at their optimal conditions and also qualitatively validate that the relative number of particles distributed across a nanocomposite is dependent on the GNS concentration and method of polymer incorporation (Figure 4). More aggregates are observed when GNS are surface-deposited atop both agarose and chitosan hydrogel (Figure 4b,d), whereas less aggregations can be seen in both GNS-embedded matrices (Figure 4a,c). Representative DFS images of the four nanocomposites at their optimal conditions also display similar GNS distribution patterns as portrayed in SEM (Figure 5). Note that the DFS and SEM images are not correlated images displaying the same field-of-view. The relative GNS distribution and aggregation patterns can be observed in diffraction-limited DFS images, and SEM images of nanocomposites provide more informative and confirmative evidence of the morphology retention and aggregation status of nanoparticles.

Proof-of-Concept SERS Mapping of Plasmonic-Polymer Nanocomposites for Sensing Applications. Plasmonic nanocomposites have been used in SERS-based sensing applications. Therefore, a proof-of-concept SERS chemical sensing study was conducted to illustrate how GNS-polymer nanocomposite fabrication conditions could influence their effective analytical performance (sensitivity as determined by SERS signal) and their reliability as an SERS substrate. The GNS-embedded agarose, GNS surface-deposited agarose, GNS-embedded chitosan, and GNS surface-deposited chitosan substrates with optimal conditions to acts as an SERS substrate for chemical detection using 638 nm laser excitation were chosen. For this SERS study, nanocomposites with a higher percentage of GNS exhibiting $\lambda_{\rm max}$ closer to 650 nm with less aggregation were used as the optimal conditions. Each

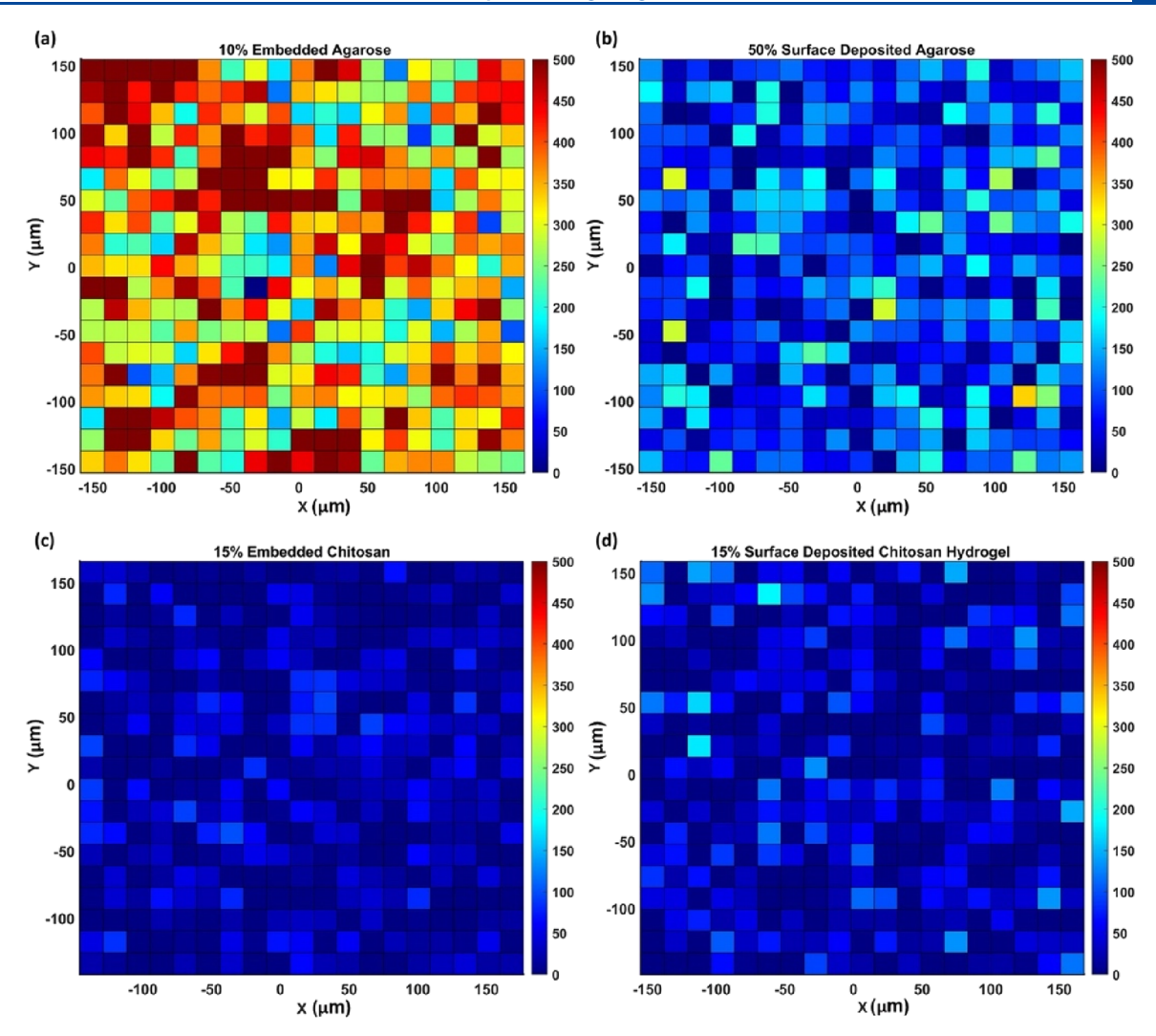


Figure 6. The effectiveness of GNS-polymer nanocomposites as SERS substrates is dictated by the analyte accessibility as governed by the polymer matrix porosity, polymer-GNS interactions, and other polymer physical characteristics. SERS maps showing the detection of rose bengal analyte using (a) 10% embedded agarose, (b) 50% surface-deposited agarose, (c) 15% embedded chitosan hydrogel, and (d) 15% surface-deposited chitosan hydrogel, which are the optimal conditions for each nanocomposite category retaining the highest percentage of GNS exhibiting scattering properties within 600–700 nm. SERS maps were reconstructed using the SERS intensity of the rose bengal characteristic peak at 1616 cm⁻¹, which was acquired using 638 nm laser, 10× objective, and laser powers of (a) 3.01 mW, (b, c)14.4 mW, and (d) 6.52 mW. Average SERS responses of the corresponding nanocomposite with no analyte (blank) were subtracted from the SERS response of the corresponding nanocomposite in the presence of the analyte and also normalized for the laser power use during spectral acquisition.

nanocomposite at the optimal conditions for SERS detection using 638 nm laser excitation was treated with 1 μ L of 10⁻⁴ M RB, and SERS mapping was done by monitoring the RB SERS response across a sample (Figures S10 and S11).

A significantly higher SERS signal intensity was observed for GNS-agarose nanocomposites than that for the GNS-chitosan nanocomposites, and GNS-embedded agarose resulted in the highest SERS signal response among all the samples. As observed by others, the shrink—swell properties of agarose during the dehydration process could lead to creating plasmonic "hot spots" by reducing the GNS proximity and also aggregation. As a result of that, RB molecules that diffuse through the agarose pores could experience high SERS enhancement, which is reflected as the high signal intensities in Figure 6a. Based on the CDF plots, while there are more aggregates that could generate "hot spots" and are present in GNS surface-deposited agarose, their LSPR is far from the 638 nm laser excitation used in this experiment, therefore providing

negligible SERS signal enhancement. This is also evident from the CDF plot, where only 13% of GNS with LSPR closer to 638 nm are present in the GNS surface-deposited agarose, while it is about 60% in GNS-embedded agarose. This difference in the percentage of GNS population appears to be a dominant factor toward the observed SERS signal intensities than the relative GNS concentration of the respective GNS-agarose nanocomposites. Relatively lower SERS signal intensities were exhibited by the GNS surfacedeposited chitosan, though the percent GNS population with LSPR closer to 638 nm laser excitation is larger (33%) than that in surface-deposited agarose (13%) (Figure 6c,d). This could be attributed to the relatively lower GNS concentrations in the optimal GNS-chitosan nanocomposite (15 v/v%) in comparison to that of agarose (50 v/v%), leading to a smaller number of GNS contributing to SERS enhancement. The lowest SERS signal intensities are shown by the GNSembedded chitosan (15 v/v%). As seen in the literature,

chitosan can form a thick protective shell around AuNPs during the nanocomposite formation, which could significantly reduce the proximity between the GNS and rose bengal (RB), the Raman-active dye. 43 As a result of that, the electromagnetic field enhancement experienced by RB in GNS-embedded chitosan nanocomposites could be minimal compared to the other three nanocomposites, thereby resulting in a much lower SERS signal response as shown in Figure 6c. This simple, proof-of-concept SERS study presents the complex interplay between the polymer type, GNS concentration, and the method of GNS incorporation into a nanocomposite affecting the optical readout from a plasmonic-polymer nanocomposite. Therefore, it is of utmost importance to consider all these factors to achieve a reasonable balance between the uniformity in GNS distribution in a polymer matrix, analyte accessibility as well as the reproducibility of optically active (SERS) substrates to ensure not only sensitive but also reproducible optical (SERS) responses. Additional SERS mapping experiments were done using RB at a lower concentration of 10⁻⁵ M (Figures S14 and S15) using the optimized nanocomposites to demonstrate possibility of detecting lower analyte concentrations. When RB analyte is added to the NP matrices, no physical polymer changes were microscopically (qualitatively) observed before and after the addition of RB analyte. The SERS maps indicated that the detection of RB at 10⁻⁵ M was possible, and similar to the SERS maps acquired using RB at 10⁻⁴ M, the SERS response of GNS-embedded and GNS surface-deposited agarose showed higher SERS responses than that of chitosan nanocomposites.

In addition, the capability of plasmonic nanocomposites in detecting hydrophobic molecules was evaluated using Nile red (10⁻⁴ M), under the same conditions used for RB detection. The SERS maps constructed using the intensity of the Nile red (NR) characteristic peak at 1487 cm⁻¹ showed that all four nanocomposites were effective in detecting hydrophobic analytes. Unlike for RB, a more hydrophilic analyte, all four nanocomposites exhibit relatively similar performance as SERS substrates toward NR (Figures S16 and S17), which could be attributed to the fact that less variation between the interactions between hydrophobic analyte and hydrophobic agarose and chitosan matrices. The average SERS intensity from NR, which is both background subtracted and normalized to the laser power, are relatively higher across all the nanocomposites in comparison to that from RB. This can be attributed to the fact that detection of RB dye (excitation wavelength = 559 nm, emission wavelength = 571 nm) was performed under non-resonant Raman conditions, while the detection of Nile red (emission wavelength in ethanol = 650 nm) by default fell under resonant Raman conditions, when the same laser excitation (638 nm) was used in SERS experiments. The SERS response of GNS-embedded agarose and chitosan hydrogel showed higher SERS responses than that of surface-deposited nanocomposites. One challenge encountered with NR was the resonant Raman condition causing high fluorescence interference and detector saturation at laser powers above 1%. Unlike more hydrophilic analytes such as RB, hydrophobic molecules like NR noticeably repelled more across and away from the more polar agarose and chitosan matrices. Overall, both GNS-agarose and chitosan nanocomposites could act as universal SERS substrates for detecting both hydrophilic and hydrophobic analytes, where more noticeable and significant variation in SERS detection

sensitivities are prevalent toward hydrophilic analytes such as RB.

CONCLUSIONS

We conducted a systematic investigation to identify the critical plasmonic-polymer nanocomposite fabrication parameters that determine the distribution of GNS and variation of their scattering properties in a polymer matrix. We identified that the identity of the polymer matrix and the method of GNS incorporation into the polymer matrix strongly dictates the stability and hence the scattering properties of GNS in a nanocomposite. While a significant change in the scattering properties of GNS was observed as a function of their concentration in the respective polymer matrices, the magnitude of λ_{max} changes is not as drastic as the other two fabrication parameters. Embedding GNS into a polymer matrix resulted in a relatively higher uniformity in GNS scattering property distribution with a lower percentage of GNS aggregation, which can be explained by GNS mixing more homogeneously and simultaneously during the gelation of both agar and chitosan. GNS-embedded chitosan hydrogel resulting in the highest overall percentage of GNS retaining optical properties can be explained by the chemical interactions between chitosan and GNS providing more nanoparticle stability and preventing aggregation. In a proof-of-concept SERS chemical detection study, we demonstrated that even small changes in the GNS concentration ($\leq 5 \text{ v/v\%}$), the method of GNS incorporation, and the polymer type could result in a drastic difference in SERS detection efficiency and their universality in detecting hydrophobic and hydrophilic analytes. Overall, our findings provide an important fundamental understanding of how the nanocomposite fabrication parameters could affect the overall optical properties of plasmonic NPs in a nanocomposite and thereby their sensitivity and reproducibility when used as optical (SERS) sensing platforms. The optimized plasmonic-polymer nanocomposite fabrication parameters presented in this study could be further refined for various plasmonic NP-polymer combinations to ensure reproducibility and reliability of their applications as optical platforms and also be extended to study varying plasmonic NP compositions and morphologies.

ASSOCIATED CONTENT

Supporting Information

The Supporting Information is available free of charge at https://pubs.acs.org/doi/10.1021/acs.langmuir.1c01826.

Synthesis and characterization of citrate-capped spherical AuNPs for seed-mediated growth of GNS, size analysis of GNS, determination of the optimal temperature for incorporating GNS into agarose, preparation of embedded and surface-deposited agarose and chitosan hydrogel at four concentration (v/v%) conditions, analysis of plasmonic-polymer nanocomposites, proof-of-concept SERS chemical detection using GNS-polymer nanocomposites (PDF)

AUTHOR INFORMATION

Corresponding Author

Agampodi Swarnapali De Silva Indrasekara — Department of Chemistry, University of North Carolina at Charlotte, Charlotte, North Carolina 28203, United States; o orcid.org/0000-0002-9731-7885; Email: adesilva@uncc.edu

Authors

- Casey Folks Department of Chemistry, University of North Carolina at Charlotte, Charlotte, North Carolina 28203, United States
- Uttam Sharma Phuyal Department of Chemistry, University of North Carolina at Charlotte, Charlotte, North Carolina 28203, United States
- Mahima Rajesh Department of Chemistry, University of North Carolina at Charlotte, Charlotte, North Carolina 28203, United States
- Nagathushara Arja Department of Chemistry, University of North Carolina at Charlotte, Charlotte, North Carolina 28203, United States
- Michael Gladden Department of Chemistry, Winthrop University, Rock Hill, South Carolina 29733, United States
- Logan Hamm Department of Chemistry, University of North Carolina at Charlotte, Charlotte, North Carolina 28203, United States

Complete contact information is available at: https://pubs.acs.org/10.1021/acs.langmuir.1c01826

Author Contributions

§C.F. and U.S.P. contributed equally to this work. A.S.D.S.I., C.F., and U.S.P., designed research and C.F., U.S.P., and M.R. conducted the nanocomposite preparation, DFS, and Raman experimentation; U.S.P. developed and conducted the DFS data analysis programs; L.H. conducted the TEM imaging; N.R. and M.G. conducted agarose gel preparation and temperature-dependence studies; and A.S.D.S.I. and C.F. wrote the paper.

Funding

This work was funded by University of North Carolina at Charlotte. The support for MG was provided by the NanoSURE REU program, which was funded through NSF Award #1757619.

Notes

The authors declare no competing financial interest.

ACKNOWLEDGMENTS

This work was performed in part at the Duke University Shared Materials Instrumentation Facility (SMIF), a member of the North Carolina Research Triangle Nanotechnology Network (RTNN), which is supported by the National Science Foundation (grant ECCS-1542015) as a part of the National Nanotechnology Coordinated Infrastructure (NNCI). The authors acknowledge the assistance of the electron microscopy facilities at Duke University in TEM and SEM imaging. Scheme ¹ and TOC were created with Biorender.

REFERENCES

- (1) De Silva Indrasekara, A. S.; Norton, S. J.; Geitner, N. K.; Crawford, B. M.; Wiesner, M. R.; Vo-Dinh, T. Tailoring the Core—Satellite Nanoassembly Architectures by Tuning Internanoparticle Electrostatic Interactions. *Langmuir* **2018**, *34*, 14617–14623.
- (2) Kim, M.; Lee, J. H.; Nam, J. M. Plasmonic Photothermal Nanoparticles for Biomedical Applications. *Adv. Sci.* **2019**, *6*, 19400471
- (3) Bouché, M.; Hsu, J. C.; Dong, Y. C.; Kim, J.; Taing, K.; Cormode, D. P. Recent Advances in Molecular Imaging with Gold Nanoparticles. *Bioconjugate Chem.* **2020**, *31*, 303–314.

- (4) Ngo, H. T.; Freedman, E.; Odion, R. A.; Strobbia, P.; De Silva Indrasekara, A. S.; Vohra, P.; Taylor, S. M.; Vo-Dinh, T. Direct Detection of Unamplified Pathogen RNA in Blood Lysate Using an Integrated Lab-in-a-Stick Device and Ultrabright SERS Nanorattles. *Sci. Rep.* **2018**, *8*, 4075.
- (5) Indrasekara, A. S. D. S.; Meyers, S.; Shubeita, S.; Feldman, L. C.; Gustafsson, T.; Fabris, L. Gold Nanostar Substrates for SERS-Based Chemical Sensing in the Femtomolar Regime. *Nanoscale* **2014**, *6*, 8891–8899.
- (6) Indrasekara, A. S. D. S.; Paladini, B. J.; Naczynski, D. J.; Starovoytov, V.; Moghe, P. V.; Fabris, L. Dimeric Gold Nanoparticle Assemblies as Tags for SERS-Based Cancer Detection. *Adv. Healthcare Mater.* **2013**, *2*, 1370–1376.
- (7) Shiohara, A.; Novikov, S. M.; Solís, D. M.; Taboada, J. M.; Obelleiro, F.; Liz-Marza, L. M. Plasmon Modes and Hot Spots in Gold Nanostar–Satellite Clusters. *Phys. Chem. C* **2015**, *119*, 10836–10843
- (8) Hamm, L.; Gee, A.; Indrasekara, A. S. D. S. Recent Advancement in the Surface-Enhanced Raman Spectroscopy-Based Biosensors for Infectious Disease Diagnosis. *Appl Sci.* **2019**, 1448.
- (9) Bodelón, G.; Montes-García, V.; López-Puente, V.; Hill, E. H.; Hamon, C.; Sanz-Ortiz, M. N.; Rodal-Cedeira, S.; Costas, C.; Celiksoy, S.; Pérez-Juste, I.; Scarabelli, L.; La Porta, A.; Pérez-Juste, J.; Pastoriza-Santos, I.; Liz-Marzán, L. M. Detection and Imaging of Quorum Sensing in Pseudomonas Aeruginosa Biofilm Communities by Surface-Enhanced Resonance Raman Scattering. *Nat. Mater.* **2016**, *15*, 1203–1211.
- (10) Moitra, P.; Alafeef, M.; Dighe, K.; Frieman, M. B.; Pan, D. Selective Naked-Eye Detection of SARS-CoV-2 Mediated by N Gene Targeted Antisense Oligonucleotide Capped Plasmonic Nanoparticles. *ACS Nano* **2020**, *14*, 7617–7627.
- (11) Link, S.; el-Sayed, M. A. Spectral Properties and Relaxation Dynamics of Surface Plasmon Electronic Oscillations in Gold and Silver Nanodots and Nanorods. *J. Phys. Chem. B* **1999**, *103*, 8410–8426.
- (12) Jain, K. P.; Lee, K. S.; el-Sayed, I. H.; el-Sayed, M. A. Calculated Absorption and Scattering Properties of Gold Nanoparticles of Different Size, Shape, and Composition: Applications in Biological Imaging and Biomedicine. *J. Phys. Chem. B* **2006**, *110*, 7238–7248.
- (13) Wu, Y.; Ali, M. R. K.; Chen, K.; Fang, N.; El-Sayed, M. A. Gold Nanoparticles in Biological Optical Imaging. *Nano Today* **2019**, 120–140.
- (14) Bolduc, R. O.; Masson, J.-F. Advances in Surface Plasmon Resonance Sensing with Nanoparticles and Thin Films: Nanomaterials, Surface Chemistry, and Hybrid Plasmonic Techniques. *Anal. Chem.* **2011**, *83*, 8057–8062.
- (15) De Silva Indrasekara, S. A.; Johnson, S. F.; Odion, A. R.; Vo-Dinh, T. Manipulation of the Geometry and Modulation of the Optical Response of Surfactant-Free Gold Nanostars: A Systematic Bottom-Up Synthesis. *ACS Omega* **2018**, *3*, 2202–2210.
- (16) Pastoriza-Santos, I.; Kinnear, C.; Pérez-Juste, J.; Mulvaney, P.; Liz-Marzán, L. M. Plasmonic Polymer Nanocomposites. *Nat. Rev. Mater.* **2018**, 375–391.
- (17) Yadid, M.; Feiner, R.; Dvir, T. Gold Nanoparticle-Integrated Scaffolds for Tissue Engineering and Regenerative Medicine. *Nano Lett.* **2019**, *19*, 2198–2206.
- (18) Matteini, P.; Ratto, F.; Rossi, F.; de Angelis, M.; Cavigli, L.; Pini, R. Hybrid Nanocomposite Films for Laser-Activated Tissue Bonding. *J. Biophotonics* **2012**, *5*, 868–877.
- (19) Gobin, A. M.; O'Neal, D. P.; Watkins, D. M.; Halas, N. J.; Drezek, R. A.; West, J. L. Near Infrared Laser-Tissue Welding Using Nanoshells as an Exogenous Absorber. *Lasers Surg. Med.* **2005**, *37*, 123–129.
- (20) Contreras-Cáceres, R.; Sánchez-Iglesias, A.; Karg, M.; Pastoriza-Santos, I.; Pérez-Juste, J.; Pacifico, J.; Hellweg, T.; Fernández-Barbero, A.; Liz-Marzán, L. M. Encapsulation and Growth of Gold Nanoparticles in Thermoresponsive Microgels. *Adv. Mater.* **2008**, *20*, 1666–1670.

- (21) Aldeanueva-Potel, P.; Faoucher, E.; Alvarez-Puebla, R.; Liz-Marzán, L. M.; Brust, M. Recyclable Molecular Trapping and SERS Detection in Silver-Loaded Agarose Gels with Dynamic Hot Spots. *Anal. Chem.* **2009**, *81*, 9233–9238.
- (22) Shan, J.; Chen, J.; Nuopponen, M.; Tenhu, H. Two Phase Transitions of Poly(N-Isopropylacrylamide) Brushes Bound to Gold Nanoparticles. *Langmuir* **2004**, *20*, 4671–4676.
- (23) Potara, M.; Maniu, D.; Astilean, S. The Synthesis of Biocompatible and SERS-Active Gold Nanoparticles Using Chitosan. *Nanotechnology* **2009**, *20*, 315602.
- (24) Ma, Y.; Chen, Y.; Tian, Y.; Gu, C.; Jiang, T. Contrastive Study of In Situ Sensing and Swabbing Detection Based on SERS-Active Gold Nanobush—PDMS Hybrid Film. *J. Agric. Food Chem.* **2021**, *69*, 1975—1983.
- (25) Ma, Y.; Du, Y.; Chen, Y.; Gu, C.; Jiang, T.; Wei, G.; Zhou, J. Intrinsic Raman Signal of Polymer Matrix Induced Quantitative Multiphase SERS Analysis Based on Stretched PDMS Film with Anchored Ag Nanoparticles/Au Nanowires. *Chem. Eng. J.* **2020**, *381*, 122710.
- (26) Tang, S.; Liu, H.; Tian, Y.; Chen, D.; Gu, C.; Wei, G.; Jiang, T.; Zhou, J. Surface-Enhanced Raman Scattering-Based Lateral Flow Immunoassay Mediated by Hydrophilic-Hydrophobic Ag-Modified PMMA Substrate. *Spectrochim. Acta, Part A* **2021**, 262, 120092.
- (27) Potara, M.; Baia, M.; Farcau, C.; Astilean, S. Chitosan-Coated Anisotropic Silver Nanoparticles as a SERS Substrate for Single-Molecule Detection. *Nanotechnology* **2012**, *23*, No. 055501.
- (28) Xu, D.; Gu, J.; Wang, W.; Yu, X.; Xi, K.; Jia, X. Development of Chitosan-Coated Gold Nanoflowers as SERS-Active Probes. *Nanotechnology* **2010**, *21*, 375101.
- (29) Kean, T.; Thanou, M. Biodegradation, Biodistribution and Toxicity of Chitosan. Adv. Drug Delivery Rev. 2010, 3-11.
- (30) dos Santos, D. S.; Goulet, P. J. G.; Pieczonka, N. P. W.; Oliveira, O. N.; Aroca, R. F. Gold Nanoparticle Embedded, Self-Sustained Chitosan Films as Substrates for Surface-Enhanced Raman Scattering. *Langmuir* **2004**, *20*, 10273–10277.
- (31) Bodnar, M.; Hartmann, J. F.; Borbely, J. Preparation and Characterization of Chitosan-Based Nanoparticles. *Biomacromolecules* **2005**, *6*, 2521–2527.
- (32) Tenório, F. S.; do Amaral Montanheiro, T. L.; dos Santos, A. M. I.; dos Santos Silva, M.; Lemes, A. P.; Tada, D. B. Chitosan Hydrogel Covalently Crosslinked by Gold Nanoparticle: Eliminating the Use of Toxic Crosslinkers. *J. Appl. Polym. Sci.* **2021**, *138*, 49819.
- (33) Raza, A.; Saha, B. In Situ Silver Nanoparticles Synthesis in Agarose Film Supported on Filter Paper and Its Application as Highly Efficient SERS Test Stripes. *Forensic Sci. Int.* **2014**, *237*, e42–e46.
- (34) Horn, C.; Pospiech, D.; Allertz, P. J.; Müller, M.; Salchert, K.; Hommel, R. Chemical Design of Hydrogels with Immobilized Laccase for the Reduction of Persistent Trace Compounds in Wastewater. ACS Appl. Polym. Mater. 2021, 3, 2823–2834.
- (35) Novo, C.; Funston, A. M.; Pastoriza-Santos, I.; Liz-Marzán, L. M.; Mulvaney, P. Influence of the Medium Refractive Index on the Optical Properties of Single Gold Triangular Prisms on a Substrate. *J. Phys. Chem. C* **2008**, *112*, 3–7.
- (36) Khoury, G. C.; Vo-Dinh, T. Gold Nanostars For Surface-Enhanced Raman Scattering: Synthesis, Characterization and Optimization. *J. Phys. Chem.* C **2008**, *112*, 18849–18859.
- (37) Nehl, C. L.; Liao, H.; Hafner, J. H. Optical Properties of Star-Shaped Gold Nanoparticles. *Nano Lett.* **2006**, *6*, 683–688.
- (38) Ma, X.; Xia, Y.; Ni, L.; Song, L.; Wang, Z. Preparation of Gold Nanoparticles-Agarose Gel Composite and Its Application in SERS Detection. *Spectrochim. Acta, Part A* **2014**, *121*, 657–661.
- (39) Vega, M. M.; Bonifacio, A.; Lughi, V.; Marsi, S.; Carrato, S.; Sergo, V. Long-Term Stability of Surfactant-Free Gold Nanostars. *J. Nanopart. Res.* **2014**, *16*, 2729.
- (40) Barbosa, S.; Agrawal, A.; Rodríguez-Lorenzo, L.; Pastoriza-Santos, I.; Alvarez-Puebla, R. A.; Kornowski, A.; Weller, H.; Liz-Marzán, L. M. Tuning Size and Sensing Properties in Colloidal Gold Nanostars. *Langmuir* **2010**, *26*, 14943–14950.

- (41) Byron, M. L.; Variano, E. A. Refractive-Index-Matched Hydrogel Materials for Measuring Flow-Structure Interactions. *Exp. Fluids* **2013**, *54*, 1456.
- (42) Fatin-Rouge, N.; Milon, A.; Buffle, J.; Goulet, R. R.; Tessier, A. Diffusion and Partitioning of Solutes in Agarose Hydrogels: The Relative Influence of Electrostatic and Specific Interactions. *J. Phys. Chem. B* **2003**, *107*, 12126–12137.
- (43) Baginskiy, I.; Lai, T.-C.; Cheng, L.-C.; Chan, Y.-C.; Yang, K.-Y.; Liu, R.-S.; Hsiao, M.; Chen, C.-H.; Hu, S.-F.; Her, L.-J.; Tsai, D. P. Chitosan-Modified Stable Colloidal Gold Nanostars for the Photothermolysis of Cancer Cells. *J. Phys. Chem. C* **2013**, *117*, 2396–2410.
- (44) Turkevich, J.; Stevenson, P. C.; Hillier, J. A Study of the Nucleation and Growth Processes in the Synthesis of Colloidal Gold. *Discuss. Faraday Soc.* **1951**, *11*, 55–75.
- (45) Rami, L.; Malaise, S.; Delmond, S.; Fricain, J.-C.; Siadous, R.; Schlaubitz, S.; Laurichesse, E.; Amédée, J.; Montembault, A.; David, L.; Bordenave, L. Physicochemical Modulation of Chitosan-Based Hydrogels Induces Different Biological Responses: Interest for Tissue Engineering. J. Biomed. Mater. Res. Part A 2014, 102, 3666–3676.
- (46) Liu, X.; Atwater, M.; Wang, J.; Huo, Q. Extinction Coefficient of Gold Nanoparticles with Different Sizes and Different Capping Ligands. *Colloids Surf.*, B **2007**, 58, 3–7.